J. Fluid Mech. (1987), *vol.* 178, *pp.* 119–136
Printed in Great Britain

Microscopic flow near the surface of two-dimensional porous media. Part 2. Transverse flow

By R. E. LARSON AND J. J. L. HIGDON
Department of Chemical Engineering, University of Illinois, 1209 W California Street, Urbana, IL 61801, USA

(Received 24 June 1986)

A model problem is analysed to study the microscopic flow near the surface of porous media. In the idealized system, we consider two-dimensional media consisting of infinite and semi-infinite periodic lattices of cylindrical inclusions. In Part 1, results for axial flow were presented. In this work results for transverse flow are presented and discussed in the context of macroscopic approaches such as slip coefficients and Brinkman's equation.

1. Introduction

In the first part of this paper, (Larson & Higdon 1986, hereinafter referred to as LH), we reviewed previous studies of flow near the boundaries of porous media concentrating on the slip condition of Beavers & Joseph (1967) and the model equation proposed by Brinkman (1947). This earlier work described the microscopic velocity field in axial flow through model two-dimensional porous media. From these results, we concluded that neither of the macroscopic approaches provided a satisfactory description for the boundary flow in porous media. The reader is referred to LH for a more complete discussion of these results. In the present effort, our goal is to extend these calculations to the more realistic problem of transverse flow through two-dimensional media. The solid geometry is identical, but the orientation of the flow has changed. Thus, the two sets of calculations provide a complete description for an arbitrary flow through these idealized two-dimensional media.

2. Mathematical formulation

We study two-dimensional Stokes flow through periodic lattices of solid inclusions. Two classes of flow are considered. The first, pressure-driven flow through doubly periodic lattices represents interior flow through the model media. These calculations investigate the effect of geometry on the permeability. The second class, simple shear flow over semi-infinite lattices represents flow over the surface of a bounded porous medium (see figure 1).

The governing equations are the Stokes equations for low-Reynolds-number flow

$$-\nabla p+\mu\nabla^2\boldsymbol{u}=0, \tag{1}$$

together with the continuity equation $\nabla\cdot\boldsymbol{u}=0$.

For an arbitrary domain, we solve these equations using the boundary-integral

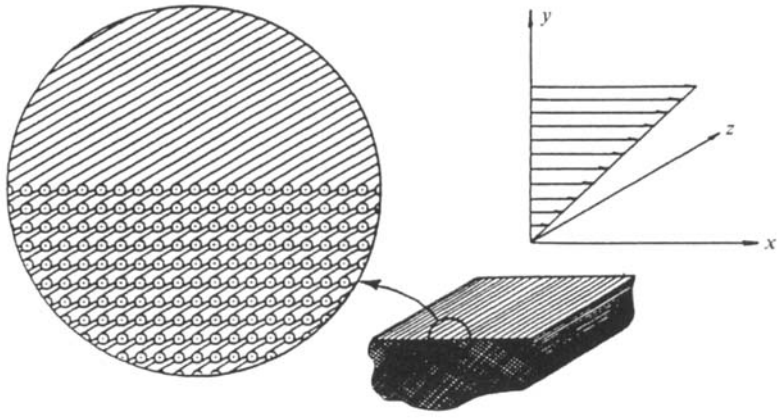

FIGURE 1. Model geometry for transverse flow over the surface of a bounded porous medium.

method described by Higdon (1985). Briefly the partial differential equations lead to the integral formula

$$u_i(\boldsymbol{x}_0) = \frac{1}{2\pi\mu}\int_S (S_{ij}(\hat{\boldsymbol{x}})f_j(\boldsymbol{x}) - T_{ijk}(\hat{\boldsymbol{x}})\,u_j(\boldsymbol{x})\,n_k)\,\mathrm{d}S, \tag{2}$$

where $\boldsymbol{u}$ and $\boldsymbol{f}$ are the fluid velocity and surface stress at points on the boundary of the domain. All symbols are as defined by Higdon (1985, equation 12) except that $\boldsymbol{n}$ points into the fluid, correcting an earlier error. The imposition of boundary conditions on $\boldsymbol{u}$ or $\boldsymbol{f}$ leads to a Fredholm integral equation for the unknown quantities. The numerical solution of these equations including error analysis and accuracy tests is discussed by Higdon.

When the boundary consists of a single continuous surface, the integral equation based on (2) provides a unique solution for the velocity, but allows an additive constant for the normal stress, i.e. the reference pressure may be prescribed arbitrarily. For a boundary consisting of several surfaces, e.g. interior inclusions, an arbitrary constant for the normal stress may be specified independently on each surface. The indeterminacy is resolved by employing the integral formula for pressure analogous to (2)

$$p(\boldsymbol{x}_0) = -\frac{1}{\pi}\int_S \left(\frac{\partial}{\partial x_j}\ln|\hat{\boldsymbol{x}}|\right) f_j(\boldsymbol{x}) - 2\mu\frac{\partial}{\partial n}\left(\frac{\partial}{\partial x_j}\ln|\hat{\boldsymbol{x}}|\right)(u_j(\boldsymbol{x}) - u_j(\boldsymbol{x}_0))\,\mathrm{d}S, \tag{3}$$

see Happel & Brenner (1973 §3–4).

With this additional equation, the pressure is determined on all surfaces to within a single constant, the reference pressure for the system. It should be noted that (3) is unnecessary if, as in the present case, we merely wish to solve (2) for the velocity in terms of a specified external pressure gradient.

Returning to the problem of flow through periodic lattices, we divide our domain into unit cells and solve (2) as an interior flow problem in each cell. The implementation of boundary conditions and continuity conditions across cell boundaries is discussed below for the two separate classes of problems.

2.1. *Boundary conditions for infinite arrays*

Consider a square lattice of circular cylinders, the simplest case among infinite arrays. The unit cell and coordinate system is shown in figure 2(*a*); the pressure gradient

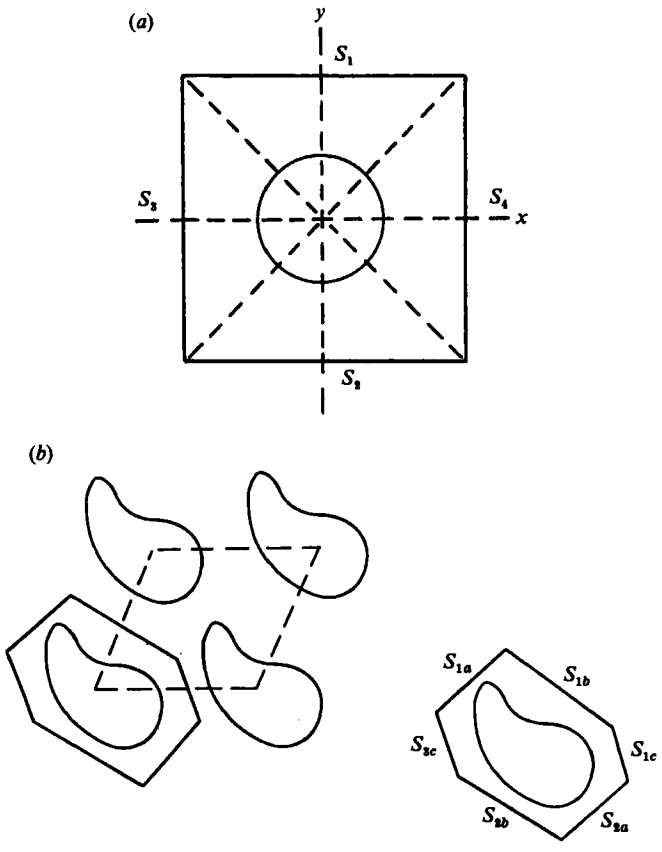

FIGURE 2. (*a*) Unit cell for an infinite square lattice of circular cylinders. Dashed lines represent symmetry planes. (*b*) Unit cell for a general lattice with arbitrary inclusions.

G is taken in the $+x$-direction, the cell width is L_0. Let $\boldsymbol{u} = (u_1, u_2)$ and $\boldsymbol{f} = (f_1, f_2)$ be the fluid velocity and surface stress respectively. For this geometry, the combination of symmetry and periodicity leads to particularly simple boundary conditions. First, on the surface of the inclusion S, we have $\boldsymbol{u} = 0$. On the top and bottom boundaries, the vertical velocity and shear stress are zero, hence $u_2 = 0, f_1 = 0$ on S_1 and S_2. On the front and back boundaries, the vertical velocity is zero, and in addition, the pressure is constant on each surface. This last condition is not immediately obvious, but follows from the Stokes equations together with the symmetries of u_2. Taking $p = 0$ at the centre of the cell, we have boundary conditions $u_2 = 0$ and $f_1 = -\frac{1}{2}GL_0$ on S_3 and S_4. Note that f_1 is $-p$ on boundary S_4, but $+p$ on boundary S_3 owing to the change in the sense of the normal vector, i.e. $\boldsymbol{n}$ points into the cell on all boundaries.

The simple form of the boundary conditions given above applies for arbitrary inclusion shapes symmetric about both the x- and y-axes in a rectangular lattice. A more general lattice is shown in figure 2(*b*). The solid boundary surface is labelled S, while the fluid cell boundary is split into two halves labelled S_1 and S_2. Segments along S_1 are related to segments along S_2 by translations corresponding to basis vectors of the lattice. It might appear that the dashed parallelogram in figure 2 would provide a simpler unit cell; however, the all-fluid cell boundary will prove more

convenient when we consider semi-infinite arrays. The no-slip condition is again $\boldsymbol{u} = 0$ on S. The periodicity conditions on the cell boundaries are now written

$$[\boldsymbol{u}]_{S_1} = [\boldsymbol{u}]_{S_2}, \tag{4}$$

$$[\boldsymbol{f} - (\boldsymbol{G}\cdot\boldsymbol{x})\boldsymbol{n}]_{S_1} = [-\boldsymbol{f} - (\boldsymbol{G}\cdot\boldsymbol{x})\boldsymbol{n}]_{S_2}, \tag{5}$$

where $\boldsymbol{G}$ is the mean pressure gradient through the lattice and may be in an arbitrary direction. The boundary condition (5) simply requires that the shear stress be periodic and that the difference in the normal stress be proportional to the pressure gradient.

2.2. *Boundary conditions for semi-infinite arrays*

We consider a simple shear flow $\boldsymbol{u}^\infty = (\dot{\gamma}y, 0)$ over a semi-infinite lattice of inclusions. The flow is periodic in the x-direction, but extends from $-\infty$ to ∞ in the y-direction. As shown in figure 3(a) for a simple square lattice, the domain covers a large number of cells above and below the interface. We proceed in a manner analogous to that used for axial flow in LH. The periodic conditions at the sides of the cell are expressed

$$[\boldsymbol{u}]_{S_3} = [\boldsymbol{u}]_{S_4}, \quad [\boldsymbol{f}]_{S_3} = -[\boldsymbol{f}]_{S_4}, \tag{6}$$

and the continuity of force and velocity at the bottom and top of each cell give

$$[\boldsymbol{u}]^i_{S_1} = [\boldsymbol{u}]^{i+1}_{S_2}, \quad [\boldsymbol{f}]^i_{S_1} = -[\boldsymbol{f}]^{i+1}_{S_2}. \tag{7}$$

The superscript indicates the cell number, where the cells are numbered consecutively from bottom to top.

At the top of the uppermost cell and bottom of the lowermost cell, the infinity conditions apply

$$[\boldsymbol{f}]_{y=+\infty} = (\mu\dot{\gamma}, 0), \quad [\boldsymbol{u}]_{y=-\infty} = (0, 0). \tag{8}$$

The no-slip condition on the solid inclusions is the same as for the infinite lattices, $\boldsymbol{u} = 0$ on S.

The simultaneous solution for the flow field in all cells would be computationally expensive. To avoid this expense, we follow LH in employing an iterative solution. Let the cell containing the top row of inclusions be labelled zero. In the first iteration, we apply the infinity conditions at the boundaries of this cell, that is

$$[\boldsymbol{f}]^0_{S_1} = (\mu\dot{\gamma}, 0), \quad [\boldsymbol{u}]^0_{S_2} = 0. \tag{9}$$

With these specifications, we calculate first approximations for $\boldsymbol{u}$ on the top and for $\boldsymbol{f}$ on the bottom of this cell. These values are used as boundary conditions on the surfaces of adjoining cells. For the first pure fluid cell, we have

$$[\boldsymbol{f}]^1_{S_1} = (\mu\dot{\gamma}, 0), \quad [\boldsymbol{u}]^1_{S_2} = [\boldsymbol{u}]^0_{S_1}, \tag{10}$$

while for the lower cell with the inclusion

$$[\boldsymbol{f}]^{-1}_{S_1} = -[\boldsymbol{f}]^0_{S_2}, \quad [\boldsymbol{u}]^{-1}_{S_2} = 0. \tag{11}$$

In each of these cells, the new values for $\boldsymbol{u}$ at the top and $\boldsymbol{f}$ at the bottom are passed in turn to the next cells, and the process continues until the upper and lowermost cell are reached.

In summary, in each pure fluid cell, the boundary conditions are

$$[\boldsymbol{f}]^i_{S_1} = (\mu\dot{\gamma}, 0) \quad [\boldsymbol{u}]^i_{S_2} = [\boldsymbol{u}]^{i-1}_{S_1}, \tag{12}$$

while in each solid cell

$$[\boldsymbol{f}]^i_{S_1} = -[\boldsymbol{f}]^{i+1}_{S_2} \quad [\boldsymbol{u}]^i_{S_2} = 0. \tag{13}$$

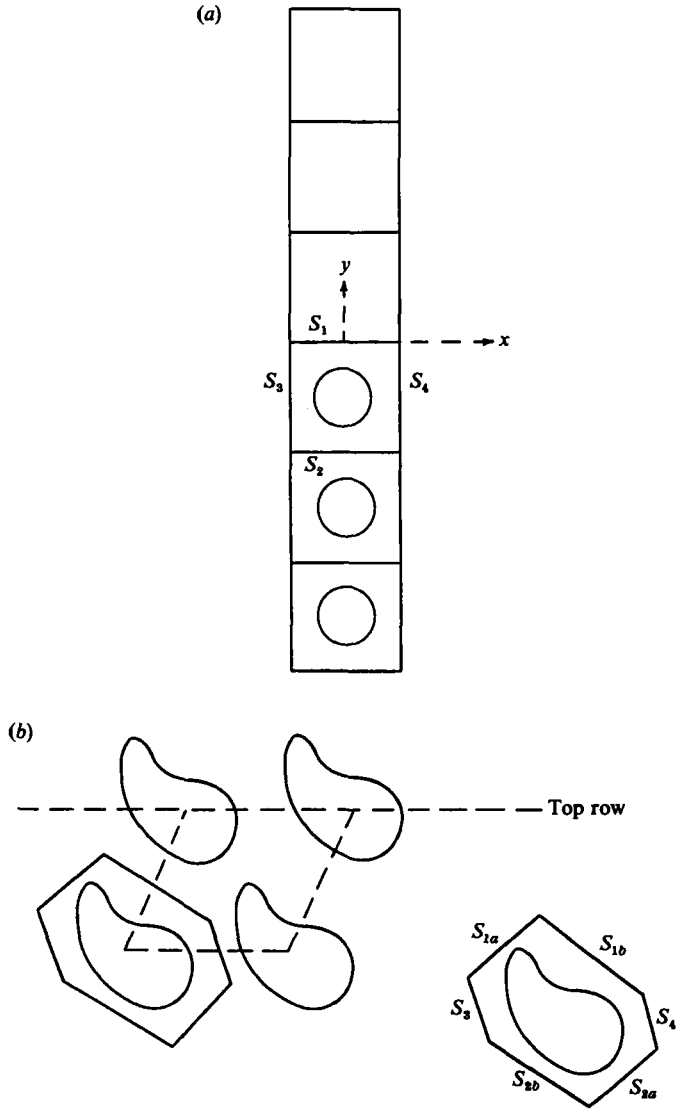

FIGURE 3. (*a*) Unit cells for semi-infinite square lattice of circular cylinders. (*b*) Unit cell for a general semi-infinite lattice.

At the start of the second iteration, we return to the zeroth cell. Instead of the infinity values, we employ the calculated values from adjoining cells in the previous iteration

$$[f]^0_{S_1} = -[f]^1_{S_2\,\mathrm{old}} \quad [u]^0_{S_2} = [u]^{-1}_{S_1\,\mathrm{old}}. \tag{14}$$

This process is repeated for all cells, and the iterations continue until convergence is achieved. In practice, we find the corrections at each iteration overcompensate, and we employ a weighted average of the old estimate and the new approximation. With this relaxation procedure, the iterations converged rapidly in all cases.

The extension of this procedure for more general lattices is straightforward. Figure 3(*b*) shows a typical unit cell with different sections of the perimeter labelled S_1 to

S_4. The periodicity boundary conditions are exactly as stated in (6). The matching conditions between adjoining cells and the steps in the iteration are also the same, the only differences being that S_1 and S_2 are slightly more general boundaries.

The method outlined above may be used to compute accurate solutions for shear flow over semi-infinite lattices; however, one additional modification is introduced. In the cells above the medium, we define disturbance quantities $\boldsymbol{u}^{\mathrm{D}} = \boldsymbol{u} - \boldsymbol{u}^{\infty}$ and $\boldsymbol{f}^{\mathrm{D}} = \boldsymbol{f} - \boldsymbol{f}^{\infty}$ and modify the boundary conditions to solve for $\boldsymbol{u}^{\mathrm{D}}$ and $\boldsymbol{f}^{\mathrm{D}}$ instead of the total quantities. This leads to a slight improvement in numerical accuracy as discussed by Higdon (1985). It should be noted that the computational cost for the interative solution of the semi-infinite lattices is comparable to the simple solution of a single cell. This feature is a consequence of the boundary-integral method as discussed in LH.

3. Transverse flow through infinite arrays

Having developed a method for solving the Stokes equations in complicated periodic domains, we first apply this technique to study the interior flow problem for model porous media. Our goal is to determine the changes in the permeability as a function of the geometrical parameters, but also to examine changes in the detailed flow field. This microscopic flow field is important for convective transport applications, and for filtration studies where individual particle trajectories are studied.

Streamlines for pressure-driven flow through a simple square lattice of circular cylinders are shown in figure 4. In the first example, figure 4(*a*), volume fraction $c = 0.10$, the streamlines form a smooth pattern with nearly equal velocity over a wide band. It is only near the cylinders and directly between them that the velocity is noticeably diminished (as shown by the spreading of the equal flux streamlines). At higher concentrations, $c = 0.40$ in figure 4(*b*), the pattern is dramatically different. The variation in velocity is now much larger with strong acceleration as the fluid squeezes through the narrow gap. In the streamwise direction, a region of separated flow has formed in the gap between cylinders. The weak eddy pattern is similar to that which has been observed for flow past an isolated pair of cylinders. It should be emphasized that the velocity in these regions is extremely small; the streamlines in these regions are drawn for clarity and are not spaced with the same flux as the main flow field. The existence of separated flow regions in a porous medium is significant, because it implies that the effective wetted surface for convective transport processes is less than the total wetted surface. In other applications, such as hydrodynamic chromatography, fine particles may migrate into the stagnant regions, leading to extremely long residence times.

Although stagnant fluid regions are important and certainly exist in real porous media, their appearance in idealized systems such as figure 4(*b*) must be interpreted with some caution. This point is clearly demonstrated in figure 4(*c*) which shows the identical medium with the direction of the pressure gradient shifted $\frac{1}{2}°$ from the x-axis. Even this minute change is sufficient to eliminate the separated region. Note that the dividing streamline is no longer symmetric and would have to be traced through a large number of cells before it reattaches to a solid boundary. Figure 4(*d*) shows the same medium with the pressure gradient oriented at an angle of 45° with respect to the x-axis. Here the flow pattern is much smoother with nearly equal velocity throughout the medium. In reviewing figures 4(*b–d*), we again note that the media are the same, and are in fact isotropic. Thus the permeability is identical in all three

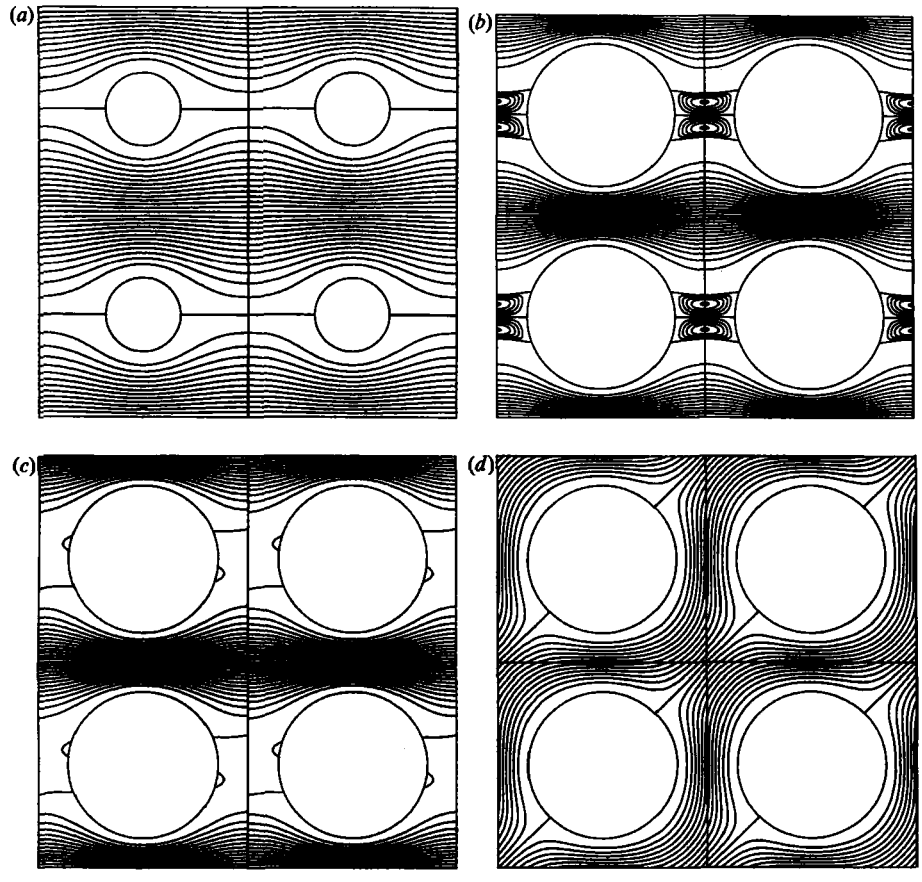

FIGURE 4. Streamlines for pressure-driven flow through infinite square lattice of circular cylinders. (*a*) Solid concentration $c = 0.10$; (*b*) $c = 0.40$; (*c*) $c = 0.40$, pressure gradient directed $\frac{1}{8}°$ from horizontal; (*d*) $c = 0.40$, pressure gradient direct at 45° to horizontal.

cases. This illustrates the fact that microscopic flow patterns may show great variation even in media which appear identical from a macroscopic point of view.

To see the effect of a different microscopic geometry, an example of a hexagonal lattice of circular cylinders is shown in figure 5. At the low concentration, figure 5(*a*), concentration $c = 0.4$ the streamlines are evenly distributed showing equal velocity. At higher concentration, $c = 0.70$ figure 5(*b*), the effect is similar to that for high concentration square arrays; that is, the main flow is confined to the clear channels with separated eddies between cylinders.

A quite different type of flow is shown in figure 6 for a square lattice of elliptical inclusions of high aspect ratio. This medium is highly anisotropic and leads to a highly skewed velocity field. The pressure gradient is horizontal, parallel to the x-axis, but the average fluid velocity is nearly parallel to the elliptical axes owing to the differences in the components of the permeability tensor.

In the streamline patterns above, we have presented a microscopic description of the porous media. For a macroscopic description, the most important property of the medium is its permeability tensor. For a general medium, it is most convenient to discuss this quantity in terms of the principal permeabilities, referred to the principal axes. The principal permeability relative to axial flow has been calculated previously

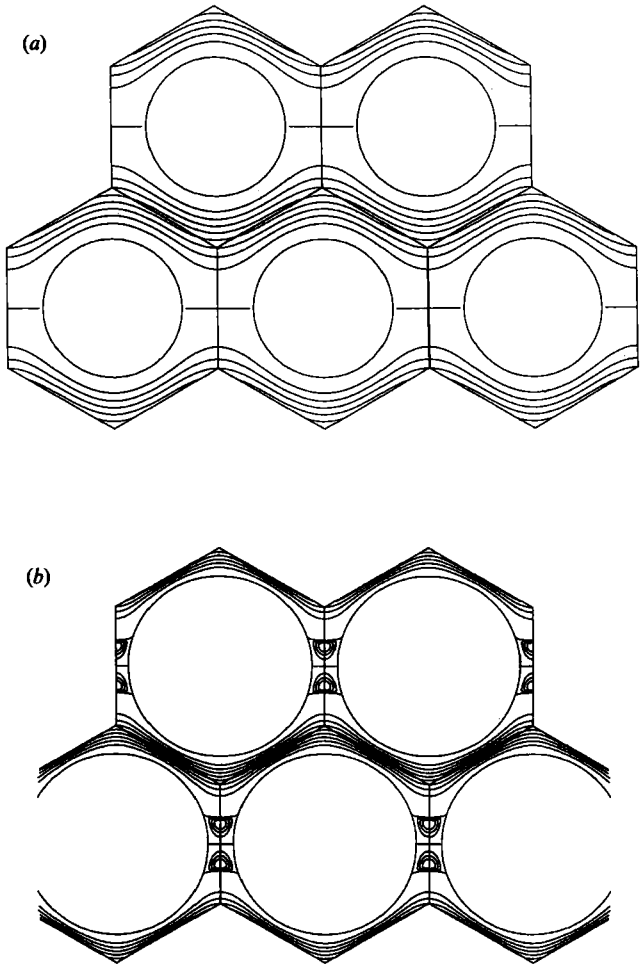

FIGURE 5. Streamlines for pressure-driven flow through infinite hexagonal lattices of circular cylinders. (a) $c = 0.40$; (b) $c = 0.70$.

in LH. For media isotropic in the transverse plane of flow, such as square or hexagonal arrays of circular cylinders, the remaining permeabilities are equal and shall be identified as k_0 in the following discussion. For anisotropic media such as illustrated in figure 6, the principal permeabilities will be identified as k_1 and k_2.

The permeability k_0 for square and hexagonal lattices of circular cylinders is shown in figure 7 as a function of concentration. This quantity has been calculated previously by Sangani & Acrivos (1982) using a different method. The two sets of calculations are in excellent agreement, providing a useful check on the accuracy. Note that the hexagonal lattice has a higher permeability but that the two values are nearly identical for small concentrations.

To investigate the effect of microscale geometry on the permeability, we examine the family of lattices studied for axial flow in LH. Specifically, consider a lattice of cylinder centres with base vectors $(L_0, 0)$ and $(H_0 \cos\theta, H_0)$. A unit cell in this lattice is a parallelogram with base L_0, height H_0 and interior angle θ. Centred on the vertices of the parallelogram are elliptical cylinders of aspect ratio a/b with major axis tilted at an angle ϕ with respect to the x-axis. The lattices thus constructed are

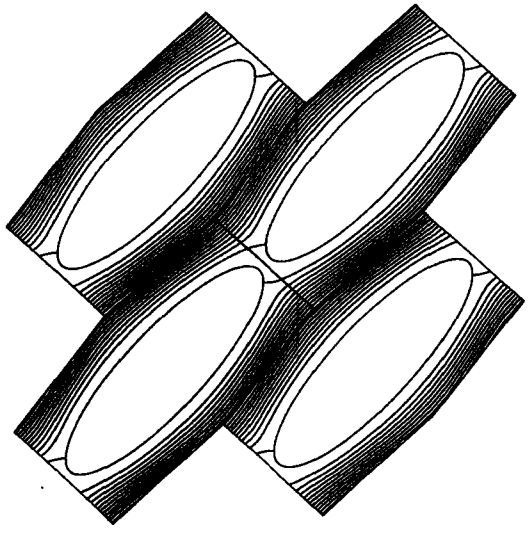

FIGURE 6. Streamlines for flow through a square lattices of elliptical cylinders. Pressure gradient is horizontal, but flow is inclined owing to strong anisotropy in the permeability tensor.

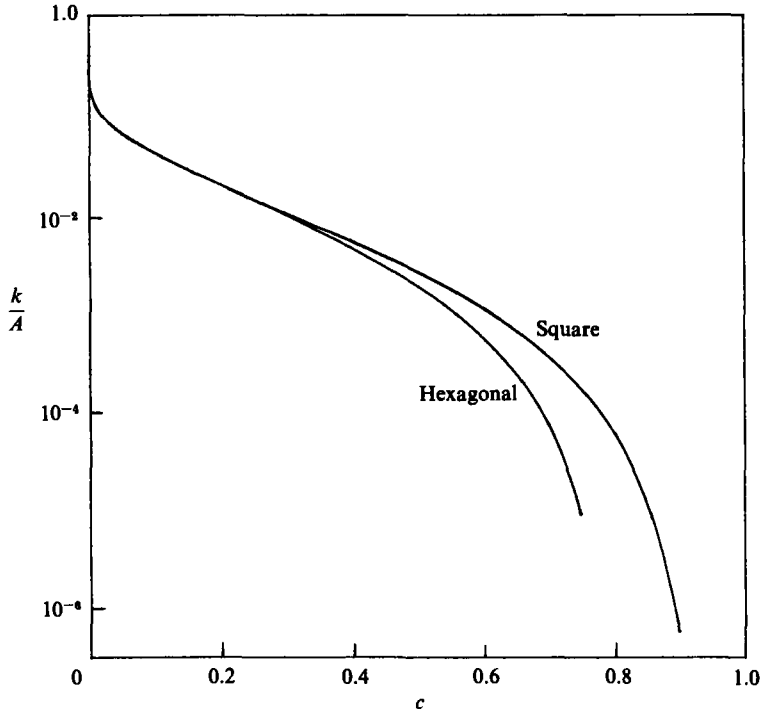

FIGURE 7. Permeability as a function of concentration for square and hexagonal lattices of circular cylinders. Permeability k normalized with respect to area of unit cell A.

characterized by the five parameters $(H_0/L_0, \theta, a/b, \phi, c)$. In the following, we calculate the permeabilities for the same types of media analysed by LH for axial flow.

The effect of lattice angle θ on the permeability is shown in figure 8 for circular cylinders at three different concentrations. The lower permeability k_2 is little affected

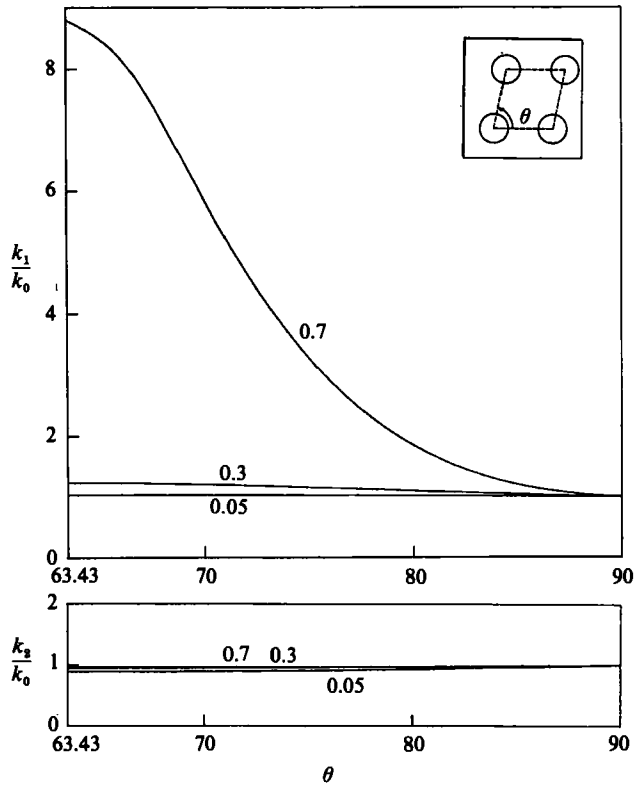

FIGURE 8. Principal permeabilities k_1 and k_2 of staggered lattices as a function of lattice inclination angle θ, normalized with respect to k_0, permeability of unstaggered lattice. Results shown for three concentrations, $c = 0.05$, 0.3 and 0.7.

by lattice angle, because the horizontal spacing between cylinders is unchanged. For the smaller concentrations, $c = 0.05$ and $c = 0.3$, the spacing between cylinders is only slightly affected, and the permeabilities k_1 are nearly equal to their respective values for the unstaggered array. For the largest concentration, $c = 0.70$, however, the stagger in the array significantly increases the gap spacing between cylinders leading to a large increase in permeability as θ departs from 90°.

The next parameter to be considered is the aspect ratio of the inclusions a/b. The permeability for a variety of lattice configurations is shown in figure 9. For all configurations, the lower permeability k_2 approaches zero with increasing aspect ratio. This result is obvious, in that the geometry is approaching a system of flat plates perpendicular to the flow direction. For most of the lattices considered (curves *b–f*) the larger permeability k_1 is only slightly affected by aspect ratio. This is explained by the fact that the slight increase in channel 'width' is offset by the increased percentage of solid surfaces on the 'sides' of the clear channel. The lone exception to this rule is lattice (*a*) which is a square lattice at concentration $c = 0.30$. For this case, the spacing between the inclusions is significantly increased, and the resulting channel 'width' leads to a sharp increase in permeability.

The importance of the inclusion tilt angle ϕ is examined in figure 10, where the permeability is plotted for three lattices with elliptical inclusions of aspect ratio $a/b = 2$. For $\phi = 0$, the lattices are very anisotropic with greater flow resistance in

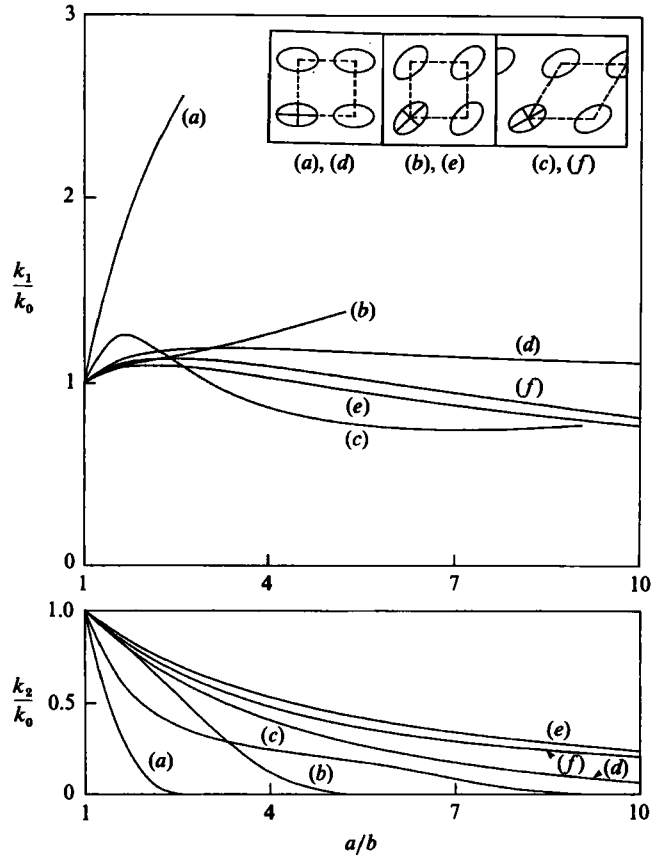

FIGURE 9. Principal permeabilities k_1 and k_2 as a function of aspect ratio a/b for elliptical inclusions in various lattice geometries, normalized with respect to value for circular cylinders.

Square lattice, $\phi = 0°$	(*a*) $c = 0.3$	(*d*) $c = 0.05$
Square lattice, $\phi = 45°$	(*b*) $c = 0.3$	(*e*) $c = 0.05$
Hexagonal lattice, $\phi = 30°$	(*c*) $c = 0.3$	(*f*) $c = 0.05$

the direction perpendicular to the major axes. As ϕ is increased, the gap spacing becomes more uniform in the principal directions and the media become more isotropic.

To summarize our results for interior flows, we have found that the microscopic flow field observed in streamline patterns may change dramatically while macroscopic measures such as permeability are unchanged. On the other hand, the macroscopic permeability may be affected by the detailed microscale geometry and is not characterized by the concentration (or porosity $\epsilon = 1 - c$) alone.

4. Transverse flow through semi-infinite arrays

As in LH, our main purpose is to describe the flow near the surface of a porous medium. Towards that goal, we consider a simple shear flow over semi-infinite lattices of inclusions. The most revealing view of this flow field is presented in the streamline patterns in figure 11 for square lattices of circular cylinders. Figure 11 (*a*) shows the flow field for a low concentration $c = 0.03$. The streamlines above the top row of

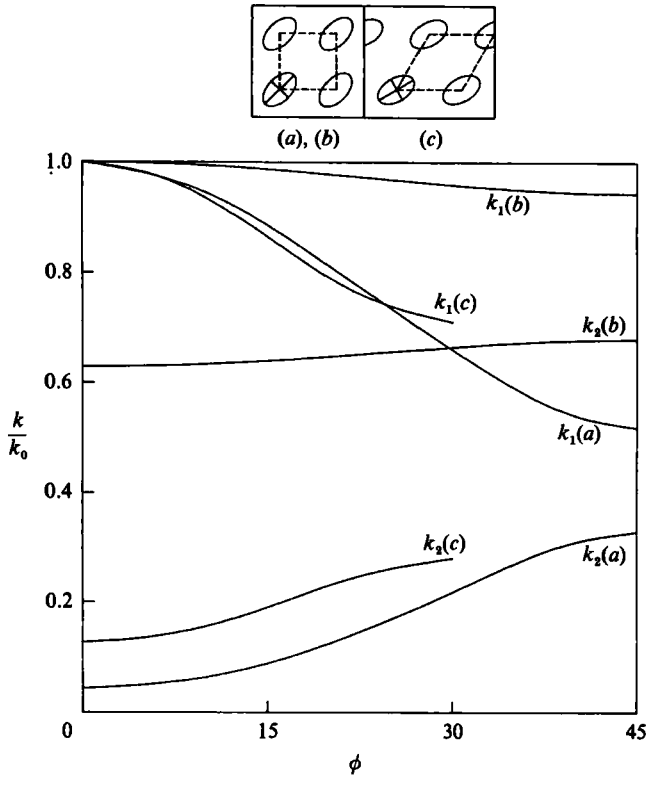

FIGURE 10. Principal permeabilities as a function of axis tilt 0 for elliptical cylinders of aspect ratio 2:1, normalized with respect to value of k_1 at $\phi = 0°$. (*a*) Square lattice, $c = 0.3$; (*b*) Square lattice, $c = 0.05$; (*c*) Hexagonal lattice, $c = 0.3$.

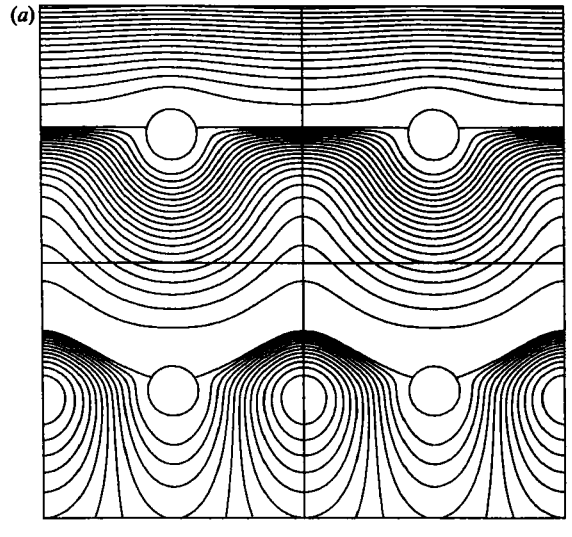

FIGURE 11 (*a*). For caption see facing page.

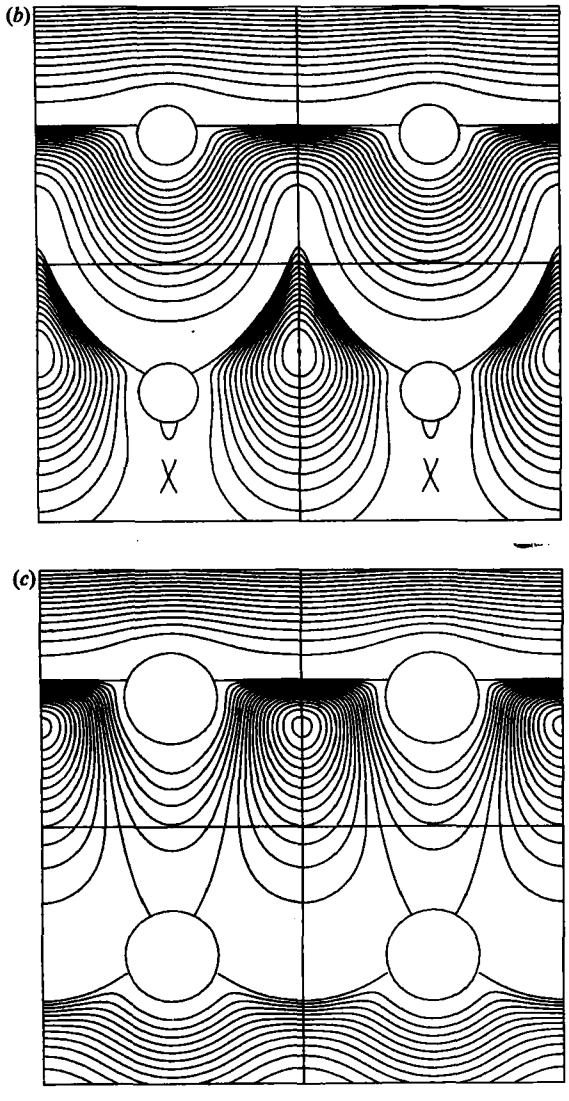

FIGURE 11. Streamlines for simple shear flow over semi-infinite lattice of circular cylinders. Figure shows top two rows of lattice. Streamlines are plotted for equal volume flow rate except at separating streamlines where streamline spacing jumps to new value to show greater detail in slower moving regions. (*a*) $c = 0.03$, (*b*) $c = 0.042$, (*c*) $c = 0.10$.

inclusions are smooth with a spacing characteristic of a slightly perturbed shear flow. In the next cell, below the top row of cylinders, the streamlines appear as one might expect, with a rapidly diminishing velocity nearly parallel to the imposed shear flow. It is in the next level that the flow changes dramatically with the appearance of a row of recirculating eddies. One layer further down (not shown here) the flow is driven in the reverse direction by the action of these eddies. Although this pattern is interesting from a mathematical and aesthetic point of view it is of little significance in physical applications. The strength of the flow field decays by two orders of magnitude over a single lattice cell. Thus, the velocity below the second row of cylinders would be negligible in any real system.

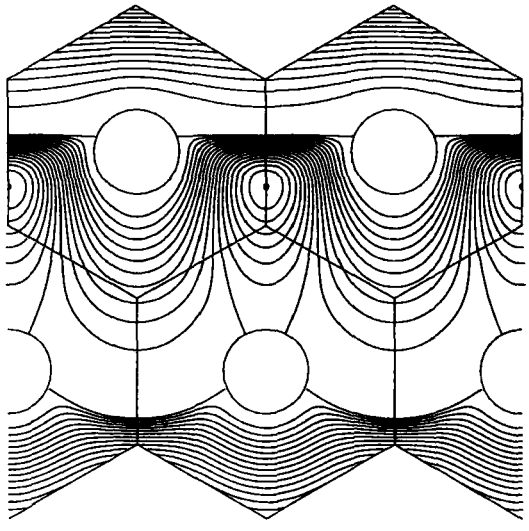

FIGURE 12. Streamlines for semi-infinite flow over hexagonal lattice of circular cylinders, $c = 0.10$.

As interesting feature of the surface flow in porous media is the change in the velocity field with small changes in the structure of the medium. Figures 11 (*b*) and (*c*) show the streamlines for square lattices with concentrations $c = 0.042$ and $c = 0.10$ respectively. Figure 11 (*b*) shows an unusual meandering flow between the first two rows of cylinders as the eddy forces its way into this region. It is also interesting to see an oblique stagnation point in the fluid below the second row of cylinders. For the higher concentration $c = 0.10$, figure 11 (*c*), the recirculating eddies appear in the first layer of the medium immediately below the top row of inclusions. As before, this drives the fluid in a reversed flow in the next layer down. For a further study of the flow sensitivity to geometry, we may examine the streamlines for a hexagonal lattice of cylinders $c = 0.10$ in figure 12. Here the eddy structure and the position of the separating streamlines have changed owing to the stagger in the rows of cylinders.

From our inspection of these streamline patterns, we conclude that the flow over the surface of a porous medium is inherently a surface phenomenon with an extremely rapid decay of velocity even at low concentrations. The flow in the first layer of the medium is not necessarily parallel to the surface but has components normal to the surface of comparable magnitude owing to the presence of recirculating eddies and regions of separated flow. Any attempt to describe this flow in terms of averaged quantities or macroscopic models will miss important details of the flow.

4.1. *Slip velocities in transverse flow*

Despite the fact that macroscopic models are inadequate for resolving the surface flow, there is continued interest in the use of slip coefficients and Brinkman's equation. We follow LH (§4.1) and show how slip velocities may be calculated for these flows. Define a nominal interface as the line intersecting the centres of the top row of inclusions. The volume flow rates Q^+ and Q^- above and below this line are calculated and used to define the slip velocity u_s as in LH. The calculation of u_s based on Q^+ is equivalent to the experimental procedure of Beavers & Joseph (1967). Slip

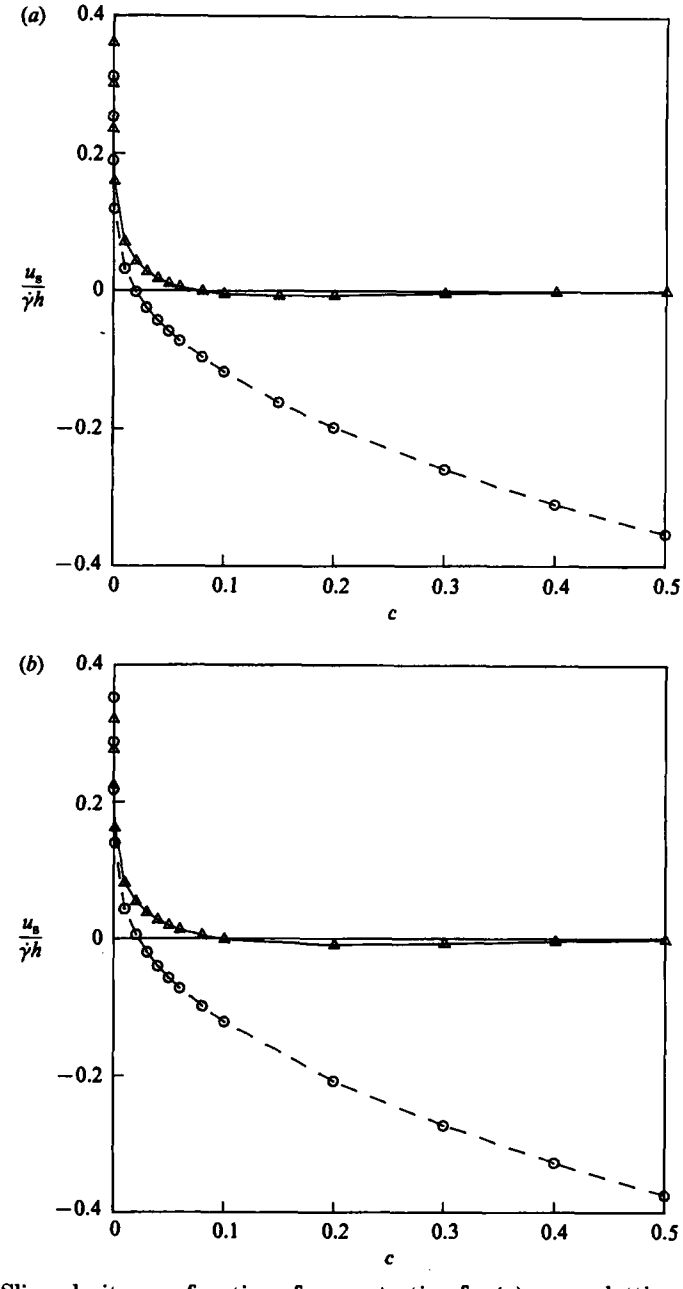

FIGURE 13. Slip velocity as a function of concentration for (*a*) square lattice, (*b*) hexagonal lattice of circular cylinders. △, is based on flow rate below interface; ○, is based on flow above interface.

velocities for square and hexagonal lattices of cylinders as a function of concentration are shown in figure 13. These results are broadly consistent with our results for axial flow through the same media. Two significant points may be reconfirmed. The first is that the two definitions of slip velocity show considerable disparity except at extremely small concentrations. The second is that the value of the slip velocity will

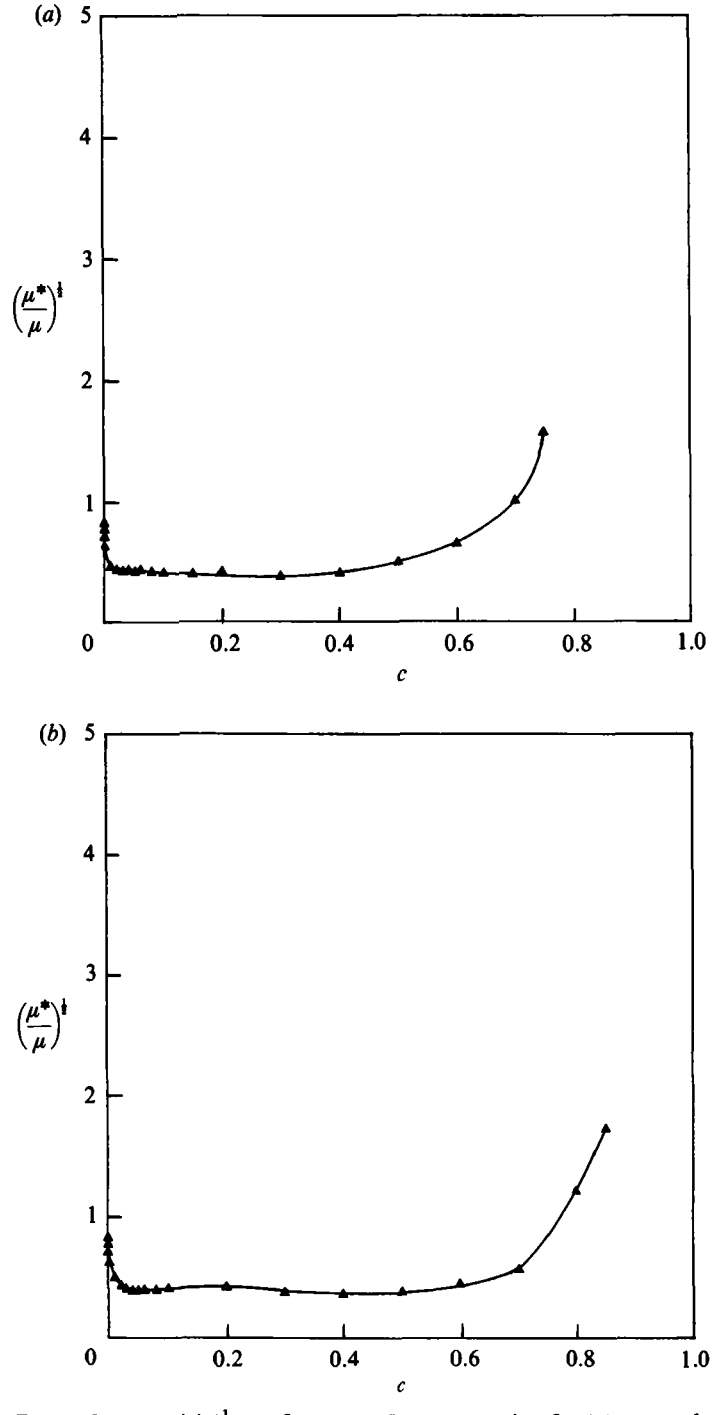

FIGURE 14. Decay factor $(\mu^*/\mu)^{\frac{1}{2}}$ as a function of concentration for (*a*) square lattices (*b*) hexagonal lattices of circular cylinders. Decay rate is calculated from the maximum shear stress on successive rows of cylinders.

be extremely sensitive to the definition of the interface as first pointed out by Saffman (1971). As an example, moving the interface a single microscopic cell length up or down changes $u_s/\dot{\gamma}h$ by ± 1.0, a variation greater than the entire range of values shown in figure 13.

4.2. *Decay factors for transverse flow*

Another macroscopic quantity which is often discussed for flow over porous surfaces is the decay factor $(\mu^*/\mu)^{\frac{1}{2}}$ based on the effective viscosity in Brinkman's equation. This is a dimensionless measure of the lengthscale for the decay of the velocity in the medium normalized with respect to the permeability. To calculate the decay factor, we require an estimate for the characteristic fluid velocity in each cell. This is difficult to achieve owing to the unusual streamline patterns and the variation with respect to concentration. For axial flow, we employed the volume flux through individual cells, however this shows strong oscillations owing to the presence of eddies. Thus, we find it most convenient to characterize the strength of the flow field by the maximum shear stress on the inclusion in each cell. Taking the ratio of this quantity from one row to the next yields a relatively smooth measure for the decay factor. This quantity is plotted in figure 14 for square and hexagonal lattices of circular cylinders. In each case, $(\mu^*/\mu)^{\frac{1}{2}}$ remains of order 1, but its numerical value shows greater variation than for the case of axial flow. This is to be expected given the drastic changes which occur in the streamlines for these media. Decay factors for more complicated geometries are not presented here. For anisotropic media, the simple idea of a decay factor is not meaningful in the context of Brinkman's equation. This point is discussed at some length in LH.

In summary, we have extended our previous calculations to include the case of transverse flow past periodic lattices as models of porous media. We have shown that the flow near the surface of a porous material may be of a quite complex nature and is sensitive to small changes in the structure of the medium. The surface-driven flow in a porous medium decays extremely rapidly even for low solid concentrations. Macroscopic models are inadequate to capture these detailed flow fields. For applications such as convective transport from porous surfaces, the microscopic flow field must be employed to calculate correctly non-linear terms such as $\boldsymbol{u}\cdot\nabla c$. The use of slip coefficients for porous boundaries is not well justified since the slip coefficient is extremely sensitive to the definition of the nominal interface. For the solution of the exterior flow field, any reasonable choice for the slip coefficient will give equivalent results with only a microscopic change in the position of the interface.

This work was supported by grants from the National Science Foundation and the Dow Chemical Company Foundation.

REFERENCES

BEAVERS, G. S. & JOSEPH, D. D. 1967 Boundary conditions at a naturally permeable wall. *J. Fluid Mech.* **30**, 197–207.

BRINKMAN, H. C. 1947 A calculation of the viscous force exerted by a flowing fluid on a dense swarm of particles. *Appl. Sci. Res.* A1, 27.

HAPPEL, J. & BRENNER, H. 1973 *Low Reynolds Number Hydrodynamics*, 2nd edn. Noordhoff.

HIGDON, J. J. L. 1985 Stokes flow in arbitrary two-dimensional domains: shear flow over ridges and cavities. *J. Fluid Mech.* **159**, 195–226.

LARSON, R. E. & HIGDON, J. J. L. 1986 Microscopic flow near the surface of two-dimensional porous media. Part 1. Axial flow. *J. Fluid Mech.* **166**, 449–472.

SAFFMAN, P. G. 1971 On the boundary condition at the structure of a porous medium. *Stud. Appl. Maths* **50**, 93–101.

SANGANI, A. S. & ACRIVOS, A. 1982 Slow flow past periodic arrays of cylinders with application to heat transfer. *Intl J. Multiphase Flow* **8**, 193–206.